npj | climate and atmospheric science

Article

Published in partnership with CECCR at King Abdulaziz University

https://doi.org/10.1038/s41612-024-00643-z

A key role of off-equatorial subsurface temperature anomalies in Tropical Pacific Decadal Variability

Check for updates

Sieu-Cuong San[1], Yu-Heng Tseng[1,2] ✉, Ruiqiang Ding[3] & Emanuele Di Lorenzo[4]

We demonstrate the key role of off-equatorial subsurface temperature anomalies in driving the phase transition of Tropical Pacific Decadal Variability (TPDV) using observation and model experiments. During the positive phase of TPDV, anomalous atmospheric responses in the off-equatorial northwestern Pacific induce positive Ekman pumping. The resulting negative subsurface temperature anomaly generated then propagates along the North Equatorial Countercurrent pathway towards the central basin, causing a sign reversal of the equatorial sea-surface temperature anomalies around three years later. Moreover, the positive phase of TPDV possibly changes the state of the Kuroshio Extension through tropical-extratropical interaction, which subsequently projects onto the footprint of the Pacific Meridional Mode, thereby amplifying subsurface-produced disturbance 0–12 months before the cold peak phase. The cold phase is completely established after five years. Similarly, the same dynamic applies to the reversed phase, leading to a preferred decadal oscillation driven by off-equatorial subsurface temperature anomalies and extratropical-tropical ocean-atmosphere interaction.

Decadal-scale sea surface temperature (SST) variability in the tropical Pacific has long been recognized as an important component of the global climate system[1–5], triggering tremendous extreme weather events globally such as droughts[6] and flooding[7]. Tropical Pacific Decadal Variability (TPDV) is generally defined as variability longer than the dominant 2–7 year timescales of El Niño-Southern Oscillation (ENSO)[8], obtained by an 8-year lowpass filtering[9,10] or 8–40 year bandpass filtering[3,5] SST in the tropical Pacific. The spatial pattern of TPDV (derived by the regression map[3]) is characterized by anomalies of one sign covering the equator and extending northeastward and southeastward toward extra-tropics, combined with anomalies of the opposite sign in the central extra-tropics of both hemispheres[3,9], resembling the pattern associated with the Interdecadal Pacific Oscillation[11] as well as ENSO[12]. However, TPDV exhibits a wider meridional extent[13,14] and shows stronger variability in the tropics than in the extra-tropics[1,3,14,15]. Recent studies have also identified that TPDV manifests the largest loadings in the equatorial central and northeastern Pacific[3,15,16], bearing resemblance to the Central Pacific El Niño[17,18] and the Pacific Meridional Mode (PMM) patterns[19,20]. In addition, some studies suggested that TPDV exhibits a prominent periodicity of around 11 years[16,21] mainly observed after 1950[21]. Therefore, our focus will be specifically on the TPDV at this timescale range.

The origin of TPDV, however, remains unclear[2,3]. Since the TPDV and ENSO share a similar structure and major episodes of decadal climate variability are well captured by the relative number of El Niño and La Niña events[3], TPDV is therefore merely regarded as the long-term linear average of the ENSO cycle[22] or the residual signal modulated by the nonlinearity of ENSO[23]. This implies that TPDV may largely originate in the tropical Pacific[16]. However, the wintertime stochastic forcings in the extratropical North and South Pacific have been put forward as the primary driver of TPDV[10,24–26]. Specifically, the tropical ocean slowly integrates the seasonal development of these remote forcings[10] in combination with positive feedbacks (zonal advective and thermocline feedback) in the tropics[24], giving rise to the TPDV. This perspective suggests that the origin of TPDV might be rooted in the extratropics. Although the proposed null hypothesis can explain the variance of decadal variability to a certain extent, it cannot account for the preferred timescale and the phase transition of TPDV.

Due to the large oceanic heat capacity, ocean dynamics have been proposed to provide the key memory for TPDV[2]. The subduction of SST anomalies in the subtropical northeastern Pacific[27] and their subsequent

[1]Institute of Oceanography, National Taiwan University, Taipei, Taiwan, ROC. [2]Ocean Center, National Taiwan University, Taipei, Taiwan, ROC. [3]State Key Laboratory of Earth Surface Processes and Resource Ecology, Beijing Normal University, Beijing, China. [4]Department of Earth, Environmental, and Planetary Sciences, Brown University, Providence, RI, USA. ✉e-mail: tsengyh@ntu.edu.tw

equatorward propagation toward the equatorial region through the subtropical-tropical cells (STCs)[28] has been hypothesized to determine the decadal timescale of Pacific climate variability[29]. However, some earlier studies suggested that these subtropical thermal anomalies decay rapidly during their propagation[30], and it is unlikely that the anomalies can reach the equator with sizeable amplitude[27]. In contrast, other studies indicated that compensating temperature and salinity anomalies (spiciness anomalies) can potentially reach the tropics, albeit with much-reduced amplitude[31]. Recently, a study has identified a decadal subsurface spiciness mode in the North Pacific associated with the Aleutian Low and Pacific Decadal Oscillation that can propagate toward the equatorial region. Nonetheless, the degree of impact that the decadal spiciness mode has on TPDV remains largely uncertain due to the negligible amplitude observed in the tropics and the relatively short observational record[5,32]. In the South Pacific, it is generally agreed that extratropical subsurface temperature/salinity anomalies can effectively propagate to the tropics on a timescale of 5–6 years and potentially contribute to equatorial climate variability[30,33,34].

Another potential driver for TPDV is the variation in the strength of STCs which may determine the decadal phase transition of equatorial SST anomalies[5,15]. The STCs encompass subtropical subduction, equatorward pycnocline flow, equatorial upwelling, and poleward surface Ekman flow[28,35,36]. An increase in the subsurface mass transport convergence of the STCs enhances the equatorial upwelling of subtropical colder waters, leading to cooler equatorial SST and shifting TPDV to the cold phase, and vice versa[37–39]. As meridional transport variability is achieved through oceanic adjustment associated with the propagation of Rossby waves[40], the preferred decadal oscillation timescale of Pacific climate can be determined by the westward propagation of wind-forced oceanic Rossby waves at specific latitudes, followed by equatorward propagation along the western boundary as coastal-trapped waves and along the equator as Kelvin waves[41]. However, the strength of the STCs is highly sensitive to both the location and magnitude of the wind forcing[40]. In addition, TPDV can contribute to extratropical wind variability through the atmospheric bridge[42–44]. Therefore, unambiguously determining the origin and preferred timescale of STCs-related mechanisms remains challenging.

Here, we demonstrate that the subsurface temperature anomalies originating in the off-equatorial northwestern Pacific can account for the phase transition of TPDV using available observational and reanalysis datasets, along with numerical experiments. Furthermore, a preferred oscillation timescale, specifically 10–20 years, can be established through the combined contribution of subsurface temperature anomalies and extratropical-tropical ocean-atmosphere interaction.

Results

Observed Pacific decadal climate variability

Prominent low-frequency variability is identified by performing bias-rectified wavelet analysis[45] of raw detrended SST anomalies averaged in the Niño4 (5°S–5°N, 160°E–150°W) and Niño3 (5°S–5°N, 150°-90°W) regions (Fig. 1b, c). Consistent with previous findings[3,16,21], the pronounced decadal variability is found in the Niño4 region, characterized by a distinct spectral peak within 8 and 16-year periods (Fig. 1b). This feature is also observed in the local fractional variance (LFV) spectrum for the combined oceanic and atmospheric fields (Supplementary Fig. 1). In contrast, there is no significant peak within the decadal band in the Niño3 region (Fig. 1c). The standard deviation of 8–20 year bandpass filtered temperature anomalies averaged between 5°S and 5°N shows significant decadal variance at depth below 50 m with two centers of action: one in the western region from 130°E to 165°E and the other in the eastern region from 170°W to 120°W[33] (Fig. 1a). These maximum variabilities are mainly confined to the isopycnals 22.5–25 σ_θ. An important feature here is that the isopycnals shoal eastward and upward (Supplementary Fig. 2a), allowing the temperature on the 22–24.5 σ_θ surfaces (thick magenta lines in Fig. 1a) to effectively affect Niño4 mixed layer temperature (Supplementary Fig. 3). The strong wavelet

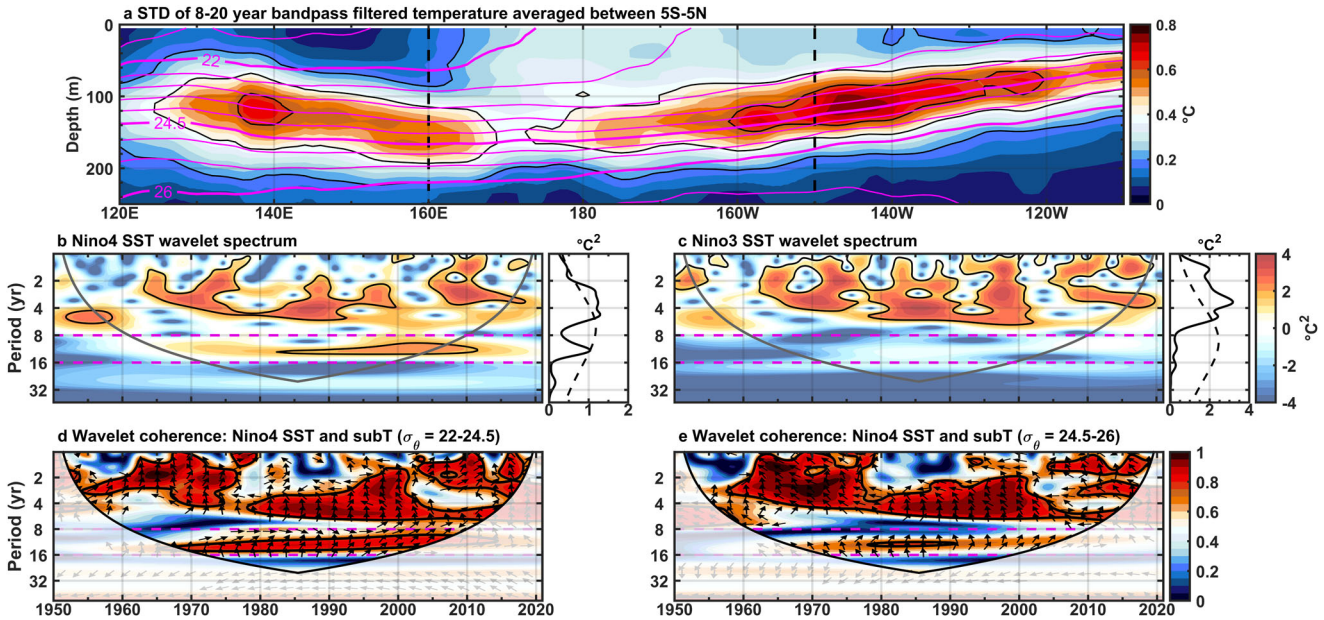

Fig. 1 | Niño4 upper ocean decadal variability. a Standard deviation of 8–20 year bandpass filtered temperature anomalies (shading and thin black contours) averaged between 5°S and 5°N. The contour interval is 0.2 °C and zero contours are omitted. Magenta lines denote the mean climatological potential density with 0.5 kg m^{-3} contour intervals. The vertical dashed black lines denote the longitude of 160°E and 150°W. **b** Bias-rectified wavelet power spectrum (shading) and corresponding global wavelet power spectrum of raw detrended Niño4 SST index. Thin black contours in the wavelet power spectrum and dashed black lines in the global power spectrum indicate statistical significance at the 90% confidence level when tested against a red-noise AR(1) process with lag-1 of 0.91. The parabola regions indicate the "cone of influence" where edge effects become important. The horizontal dashed magenta lines indicate the 8 and 16-year periods. **c** Same as (**b**) but for Niño3 SST index. Wavelet coherence between Niño4 SST index and Niño4 subsurface temperature anomalies averaged between (**d**) 22–24.5 σ_θ and (**e**) 24.5–26 σ_θ. The 95% significance level against red noise is shown as thick black contours. The vectors indicate the relative phase relationship (pointing right indicates in phase, pointing left indicates out of phase, and pointing vertically upward means the Niño4 SST index lags subsurface temperature by 90°). The horizontal dashed magenta lines are the same as (**b**).

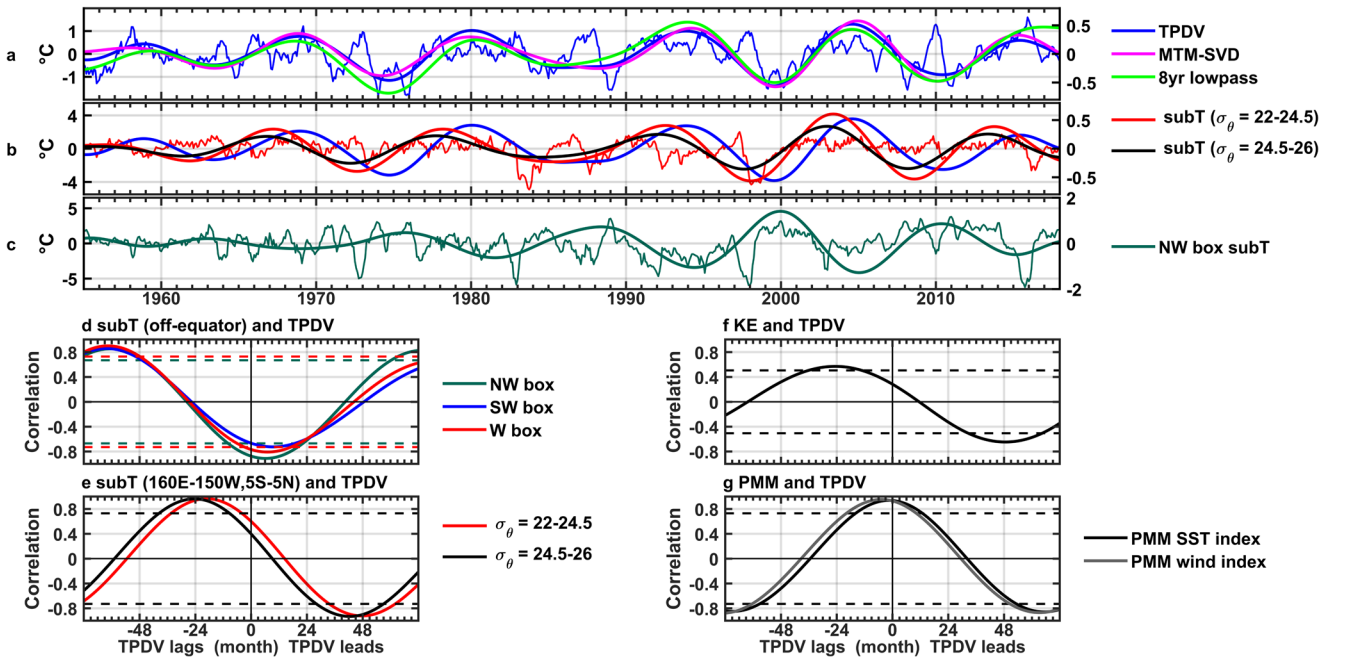

Fig. 2 | Subsurface temperature anomalies lead the phase reversal of Tropical Pacific Decadal Variability (TPDV). a Temporal evolution of raw detrended Niño4 SST index (left axis, thin blue) and its (right axis, thick blue) 8–20 year bandpass filtered component (TPDV index), and (right axis, green) 8-year lowpass filtered component. The reconstructed Niño4 SST index using the MTM-SVD method on a decadal timescale (period ~10.3 years) is shown in magenta (right axis). **b** Temporal evolution of raw detrended Niño4 subsurface temperature anomalies averaged between 22 and 24.5 σ_θ (left axis, thin red) and its reconstruction using MTM-SVD on a decadal timescale (right axis, thick red). Similarly, the reconstruction of Niño4 subsurface temperature anomalies averaged between 24.5 and 26 σ_θ is shown in black (right axis). The blue line is the same as (**a**). **c** Temporal evolution of raw detrended subsurface temperature anomalies averaged between 22 and 24.5 σ_θ in 6°–11°N, 140°–160°E (NW box in Fig. 3) (left axis, thin green) and its 8–20 year bandpass filtered component (right axis, thick green). Lead-lag correlation coefficients between TPDV index and (**d**) 8–20 year bandpass filtered temperature anomalies averaged between 22 and 24.5 σ_θ in (green) NW box, (blue) 6°–11°S, 150°–170°E (SW box) and (red) 5°S–5°N, 150°–160°E (W box), (**e**) reconstructed Niño4 subsurface temperature anomalies averaged between (red) 22–24.5 σ_θ and (black) 24.5–26 σ_θ using the MTM-SVD, (**f**) 8–20 year bandpass filtered KE index defined as area-averaged SSH anomalies in 31°S–36°N, 140°–165°E and (**g**) 8–20 year bandpass filtered PMM (black) SST and (gray) wind index. Horizontal dashed lines in (**d**–**g**) show the 95% confidence level based on the non-parameter random-phase test.

coherence between Niño4 SST and Niño4 subsurface temperature averaged between 22 and 24.5 σ_θ further demonstrates the close connection between the surface and subsurface oceanic variability at the decadal timescale (Fig. 1d). In addition, the relative phase relationship (indicated by arrows) suggests that subsurface temperature leads SST variability by approximately 45° at periods greater than eight years. The deeper isopycnal temperature anomalies also exhibit a qualitatively similar relationship (Fig. 1e), but the coherence is not statistically significant compared to the upper layer (Fig. 1d).

As decadal variability centering in the equatorial central Pacific, here we define a TPDV index using an 8–20 year bandpass filtered Niño4 SST anomalies to describe the physical processes responsible for the variation (similar results are obtained if an 8 year lowpass filtering or Multitaper Frequency-Domain Singular Value Decomposition (MTM-SVD) is used, Fig. 2a). The temporal evolution of the Niño4 22–24.5 σ_θ temperature anomalies extracted by the MTM-SVD displays pronounced feature of decadal variability (Fig. 2b). Its variation exhibits a larger magnitude compared to the lower isopycnal level (thick red and black lines in Fig. 2b), consistent with the wavelet coherence analysis in Fig. 1. Moreover, the maximum values of the temperature anomalies between 22 and 24.5 σ_θ lead the peaks of the TPDV index by months (correlation reaches 0.96 by 19 months in Fig. 2e), in agreement with the relative phase relationship in Fig. 1d. Therefore, upper oceanic variability emerges as a potential precursor of TPDV which will be further examined next. The temperature between 24.5 and 26 σ_θ also shows a strong and consistent correlation with TPDV, confirming the key role of subsurface temperature on the TPDV. For simplicity, we focus entirely on the 22–24.5 σ_θ in the following analysis unless otherwise noted.

The decadal evolution of surface oceanic and atmospheric fields reconstructed from MTM-SVD illustrates a completed phase transition of TPDV (Fig. 3). During the positive phase of TPDV (Fig. 3a), the largest SST loadings are observed in the Niño4 region and northeastern Pacific[4,18]. This characteristic is consistent with previous studies based on MTM-SVD analysis of combined SST, sea surface height (SSH), and tropical subsurface temperature anomalies above 350 m[16], and the regression pattern of bandpass filtered SST anomalies on the first principal component of the leading empirical orthogonal function of the 8 to 40-year band SST anomalies[3]. The decadal sea level pressure (SLP) pattern is characterized by a band of anomalous high SLP anomalies confined to the western side of the basin while anomalous low pressure dominates in the east, especially in the extratropics. The latter structure resembles the Aleutian Low, suggesting possible atmospheric teleconnections excited by TPDV[20,46,47]. The circulation patterns in the extratropical Northern and Southern Hemispheres are similar to those associated with the North[20] and South[48] PMM, respectively. In addition, associated with the equatorial warm SST anomalies, strong westerly winds are observed west of 150°W while northwesterly and southwesterly winds dominate in the off-equatorial northwestern and southwestern Pacific, respectively. In general, the ocean-atmosphere interaction during the positive phase is consistent with a typical Gill-type response in the off-equatorial northwest and southwest[49] resulting from the strong positive SST anomalies in the equatorial central Pacific. The corresponding positive (negative) wind stress curl anomalies in the 2–15°N (2–15°S) latitudinal band (Supplementary Fig. 4a) then induce positive Ekman pumping (Supplementary Fig. 4b), leading to the formation of subsurface temperature

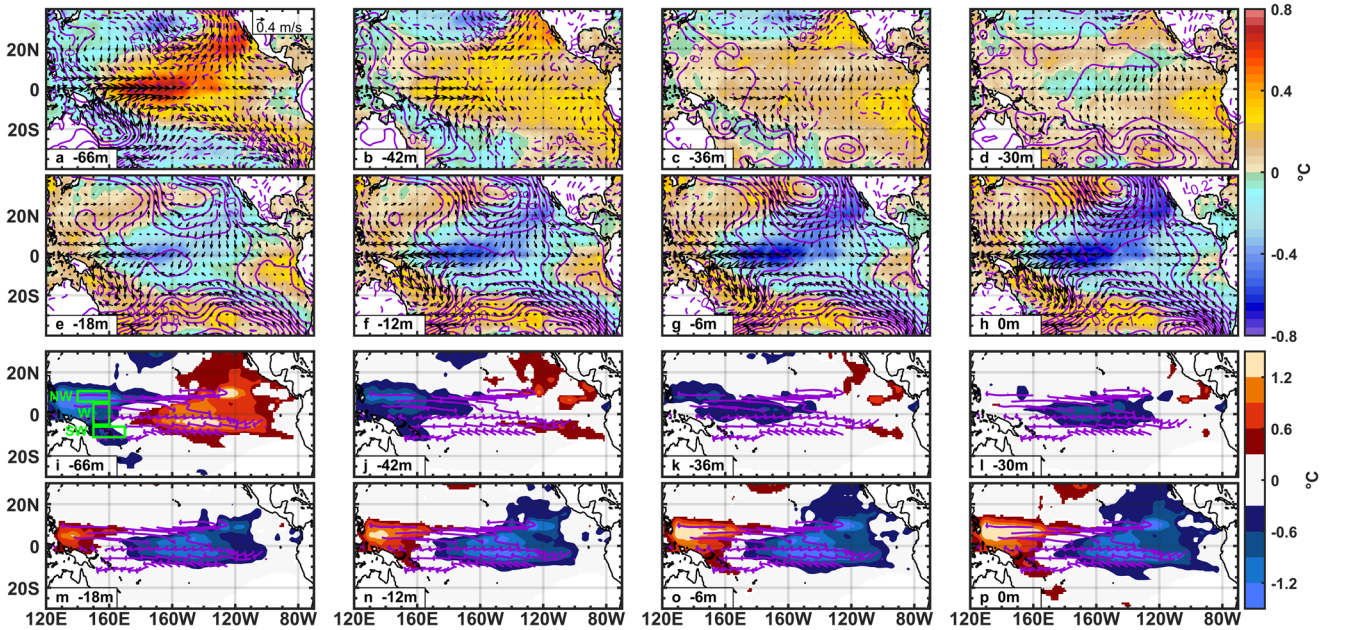

Fig. 3 | Off-equatorial northwestern subsurface temperature anomalies initiate the phase reversal of Tropical Pacific Decadal Variability (TPDV). a–h Phase evolution of Pacific SST (shading), SLP (contours, hPa), and 10-m wind vector anomalies on decadal timescales (period ~10.3 years in the MTM-SVD analysis). The contour interval is 0.1 hPa (positive/negative is solid/dashed). **a**, **h** correspond to positive and negative phases of TPDV, respectively. **d** Corresponds to the phase reversal. The numbers indicate the evolution of the fields in months before the peak cold phase, for example, -6 m indicates 6 months before the peak of the cold phase. **i–p** Same as (**a–h**) but for subsurface temperature anomalies averaged between 22 and 24.5 σ_θ. For clarity, positive (negative) temperature anomalies greater (smaller) than 0.3(−0.3) °C have been colored in red (blue). Vectors denote the mean current on 23.5 σ_θ derived from GODAS during 1980–2021. Only some representative current vectors are shown. The green rectangles in (**i**) are the regions defined in Fig. 2.

anomalies in the off-equatorial northwestern and southwestern Pacific, respectively (the two green boxes in Fig. 3i). This will be further examined in the next section.

Before evolving into the mature cold phase (Fig. 3h), negative PMM-like patterns occur in the extratropics concurrent with the strengthening of negative SST in the equatorial central and northeast Pacific (Fig. 3e–h). Previous studies have indicated that these meridional modes, also described as seasonal footprinting mechanism[50,51], can contribute to equatorial low-frequency variability around 0–12 months before the mature state[10,24] (consistent with Fig. 2g). The regression of SST anomalies upon the filtered PMM SST index (similar result obtained for PMM wind index) further confirms the role of PMM in enhancing SST variance around one year before the peak phase of TPDV (Supplementary Fig. 5g, h).

But how can the PMM be formed during the transition state to contribute to the growth of TPDV? Apart from the contribution from internal stochastic forcing in the midlatitude[52–54] and East Asian winter monsoon[55], many previous studies have suggested that atmospheric teleconnection during the peak phase of TPDV can drive changes in the Aleutian Low or NPO on a timescale of 1–3 months[42–44]. The resulting atmospheric variability associated with the Aleutian Low/NPO then excites westward propagating oceanic Rossby waves that affect the Kuroshio Extension (KE) system after 2.5–3 years[25,56–58]. The change in the KE state then induces a persistent downstream atmospheric response that subsequently projects onto the forcing pattern of the PMM (around 0–12 months) and drives some fraction of equatorial low-frequency variability[25]. Consistent with previous finding[25], the lead-lag correlation between the filtered KE index (defined as area-averaged SSH anomalies in the 31°S–36°N, 140°–165°E[59]) and the TPDV index exhibits a sinusoidal pattern in which the former leads the latter by two years, while the latter can also provide feedback to the former after three to four years (Fig. 2f). The regression of SST anomalies upon the filtered KE index when the latter leads further demonstrates that the KE can induce a weak but still significant fraction of low-frequency SST variability in the tropics (Supplementary Fig. 5a–d). In addition, the atmospheric structure associated with the KE can explain a certain degree of the PMM pattern (compare contours in Supplementary Fig. 5). As a result, the state change of the KE partially excites the PMM[59–63] to further strengthen the low-frequency SST variance (Fig. 3f–h and Supplementary Fig. 5).

The above observed Pacific climate variability is consistent with the established decadal framework so far[24,25]. However, neither the KE nor the North and South PMM can fully explain the phase reversal of TPDV (note that KE primarily induces equatorial SST anomalies through the PMM pathway[25], Supplementary Fig. 5). In addition, northeastern subtropical SST anomalies nearly in-phase with equatorial central Pacific SST variability at the decadal timescale, suggesting that the subtropical PMM might not be the primary driver of the decadal phase reversal of TPDV[16]. In the next section, we will demonstrate that the equatorial emergence of subsurface temperature anomalies originating in the off-equatorial northwestern Pacific can trigger the phase reversal of TPDV. Specifically, by combining these off-equatorial subsurface temperature anomalies with the extratropical-tropical ocean-atmosphere interaction framework, we can establish the preferred decadal timescale oscillation in the Pacific.

Origin and preferred timescale of TPDV

The significant warming observed in the equatorial central Pacific during the positive phase of TPDV suggests a Gill-type response in the tropical Pacific, leading to the formation of subsurface temperature anomalies in the off-equatorial western Pacific[49]. Could the underlying water in the off-equatorial western Pacific potentially cause the phase reversal of TPDV? Fig. 3i–p shows the phase evolution of upper ocean temperature anomalies reconstructed from MTM-SVD, which generally bears resemblance to those associated with surface variability. One important feature is the occurrence of a strong negative signal in the off-equatorial western Pacific, centered around 6–11°N (Fig. 2c) which has the opposite sign to the Niño4 SST anomalies during the positive TPDV mature phase (Fig. 3a, i). In addition, subsurface anomalies precede surface variability in the western-central equatorial region during the reversal state (Fig. 3d, e, l, m) around 3 years later, consistent with the correlation analysis in Fig. 2e. Figure 2d shows the lead-lag correlation between filtered area-averaged subsurface temperature

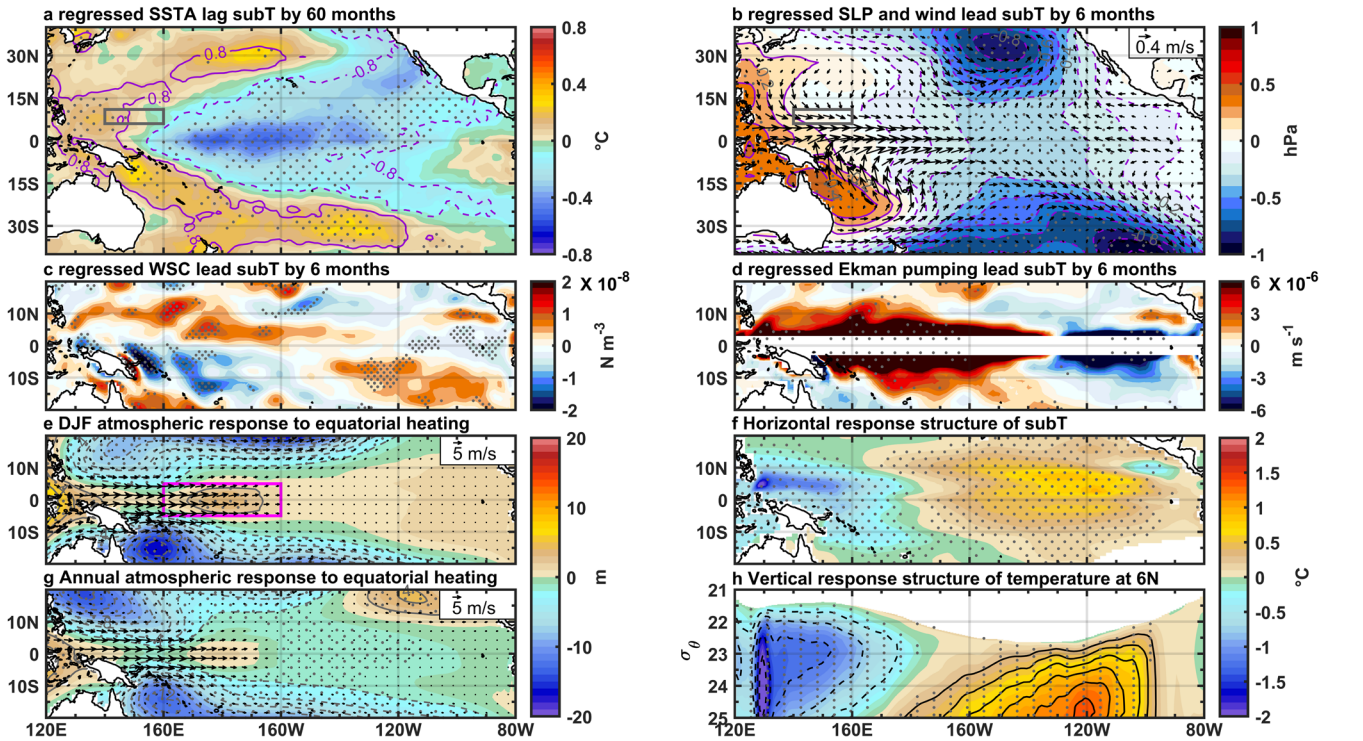

Fig. 4 | Gill-response in the off-equatorial northwestern Pacific forces subsurface temperature anomalies. 8–20 year bandpass filtered temperature anomalies averaged between 22 and 24.5 σ_θ in NW box (gray rectangle) regressed with 8–20 year bandpass filtered (**a**) SST, (**b**) SLP (shading, contour, and stipple) and 10-m wind anomalies, (**c**) wind stress curl and (**d**) Ekman pumping. In (**a**) contours are the correlation coefficients between 8 and 20 year bandpass filtered NW box subsurface temperature anomalies and 8–20 year bandpass filtered SST anomalies. The contour interval is 0.2 and only correlation coefficients greater than 0.8 are shown. The contour interval in (**b**) is 0.1 hPa (positive/negative is solid/dashed). Regressed wind vectors are shown as a whole for clarity. Stipples indicate the region exceeding 95% confidence level with the random-phase test. **e** Wintertime (December–February) and (**g**) annual response of 850 hPa geopotential height (shading and contour) and 850 hPa winds with specified 2 °C SST anomalies imposed in the magenta rectangle region shown in (**e**). **f** Annual horizontal response structure of temperature averaged between 22 and 24.5 σ_θ to the superimposed anomalous wind fields associated with the positive phase of the TPDV. **h** Same as (**f**) but for longitude- σ_θ plot of the response of temperature at 6°N. Stipple indicates 95% significance level based on a Student's *t* test.

anomalies in the western Pacific (three green boxes in Fig. 3i, NW, W, SW from north to south) and the TPDV index. All correlations exhibit a sinusoidal shape with extremely high crests and troughs, suggesting a strong coupling between the western subsurface temperature anomalies and equatorial SST variability at the decadal timescale. Specifically, the correlation between subsurface temperature anomalies averaged over the off-equatorial northwest region (NW box) and TPDV reaches as high as 0.84 by 60 months when the former leads. Additionally, the TPDV shows a much stronger correlation with NW subsurface temperature anomalies by about six months. This can establish a preferred decadal oscillation identified so far.

We further quantify the subsurface contribution to TPDV by regressing the filtered area-averaged temperature anomalies between 22 and 24.5σ_θ in the NW box (the largest loading in Fig. 3i) upon the filtered SST anomalies (Fig. 4a). As expected, the strong negative subsurface temperature anomalies originating in the NW region can explain significant low-frequency variance in the Niño4 region five years later (Figs. 3h and 4a). Note that the contribution from the subsurface is of greater magnitude than that from the KE during the transition phase (Fig. 4a and Supplementary Fig. 5a, b). Therefore, off-equatorial subsurface temperature anomalies may be the primary contributor to the phase reversal of TPDV.

But how can the strong negative temperature anomalies approach the central basin and trigger the phase reversal of TPDV? The evolution in Fig. 3 suggests that negative subsurface temperature anomalies in the NW box progress gradually eastward and equatorward, following the mean current (violet vectors) toward the central basin. This process aligns with the shallow North Equatorial Countercurrent (NECC) pathway which can be defined by the acceleration potential evaluated on isopycnal surfaces (Fig. 5a–f). Lagrangian particle-tracking experiments provide additional evidence confirming the existence of the NECC pathway (see Methods). The timescale for a particle originating in the off-equatorial northwestern Pacific to reach the Niño4 region is approximately 1.5–3 years, depending on the evaluated isopycnal surface (Supplementary Fig. 6). Specifically, the advection speed is fast near the surface (Supplementary Fig. 6a), progressively decelerating at greater depths (Supplementary Fig. 6d). The propagation timescale from our tracer experiments is consistent with the advection timescale in Fig. 3.

The reconstructed temperature anomalies using MTM-SVD averaged in 6°N illustrate the propagation characteristic along the NECC pathway from around 140°E to 160°W (Fig. 5g, shading) while the reconstructed signals on the equator can only reach as far as 170°E (Fig. 5g, contours). Moreover, the signal along 6°N is much stronger and more coherent than those at the equator. The NW subsurface temperature anomalies lead to the observed decadal SST variability in the Niño4 region (Fig. 5h, i), consistent with the correlation analysis in Fig. 2. As a result, the gradual migration of NW subsurface temperature anomalies toward the dateline via the NECC pathway can effectively determine the preferred timescale and the phase reversal of TPDV. This is facilitated by the eastward shoaling of the examined isopycnal range (Supplementary Fig. 2a), which allows the outcropped subsurface temperature anomalies to directly affect surface temperature variability (Supplementary Fig. 3), thus triggering the phase reversal (Fig. 3d) and inducing significant low-frequency variance in the Niño4 region (Fig. 4a). The propagation pathway from the NW region to the equatorial Pacific are consistent with previous studies based on a shallower isopycnal level[64] or depth-averaged temperature anomalies[65].

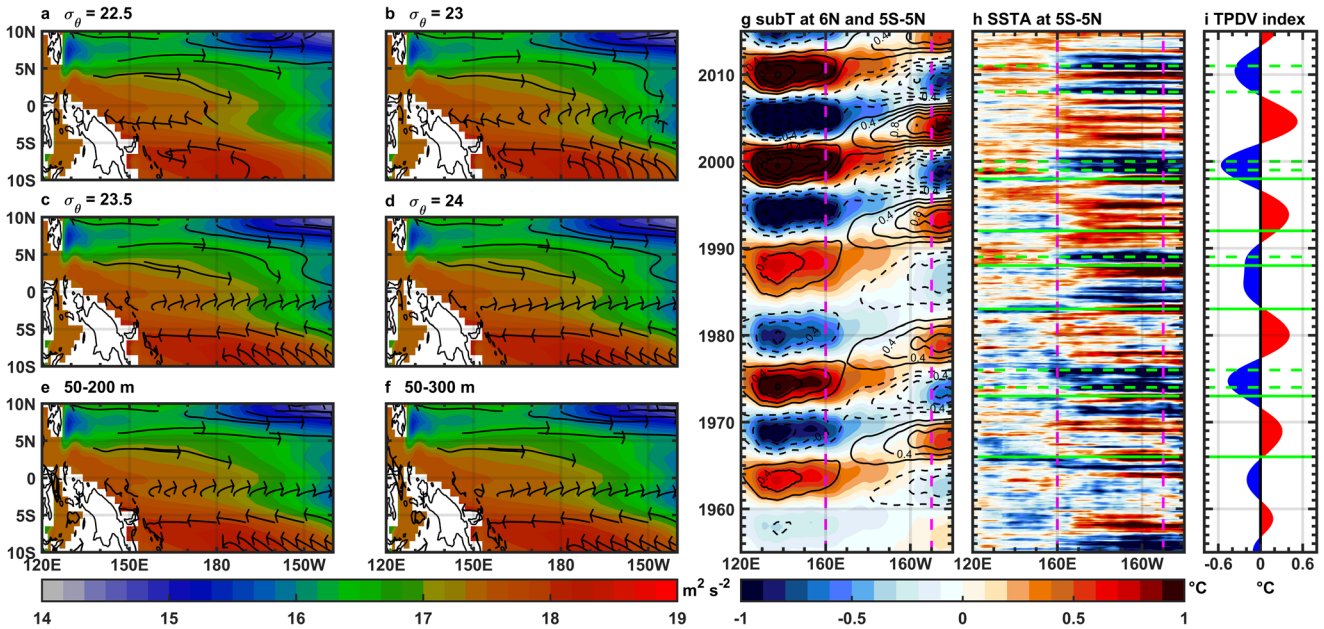

Fig. 5 | Off-equatorial northwestern Pacific subsurface temperature anomalies propagate to the central basin via the NECC pathway. Mean acceleration potential (shading) referenced to 1000 dbar evaluated on 23.5 σ_θ and mean current vectors evaluated on (**a**) 22.5 σ_θ, (**b**) 23 σ_θ, (**c**) 23.5 σ_θ, and (**d**) 24 σ_θ. (**e, f**) Same as (**a**–**d**) but for mean depth-integrated current vectors between (**e**) 50–200 m and (**f**) 50–300 m. Only some representative current vectors are shown. **g** Reconstructed subsurface temperature anomalies between 22 and 24.5 σ_θ using MTM-SVD averaged along 6°N (shading) and 5°S–5°N (contour). The contour interval is 0.2 °C (positive/negative is solid/dashed). **h** SST anomalies averaged between 5°S and 5°N. **i** TPDV index. The vertical dashed magenta lines indicate the longitude of 160°E and 150°W. The horizontal solid (dashed) green lines indicate strong and very strong El Niño (La Niña) events that peak in December based on the Oceanic Niño Index (ONI). SST anomalies in (**h**) are obtained by removing the linear trend and the climatological monthly mean over 1950–2020.

We then examine how subsurface temperature anomalies are formed in the off-equatorial western Pacific at the decadal timescale. The mean advection of extratropical spiciness anomalies[32,66] and wind-forced thermocline displacement have been proposed[67]. To assess the role of remote spiciness advection, the standard deviation of filtered subsurface temperature anomalies averaged between 22 and 24.5 σ_θ (temperature interpolated to time-varying isopycnals) is shown in Supplementary Fig. 7a. The results indicate that decadal variability due to the mean advection of spiciness anomalies is weak in the off-equatorial western Pacific. There is only one noticeable center of action in the equatorial western Pacific around 140°E that cannot fully account for the observed large subsurface temperature variability (Fig. 3i). However, large spiciness variabilities are observed in the central-eastern equatorial and southeast Pacific (Supplementary Fig. 7a). On the other hand, the spatial structure of the standard deviation of the filtered isopycnal depth anomalies averaged between 22 and 24.5σ_θ indicates that a large portion of off-equatorial temperature anomalies results from the vertical displacement of the thermocline (Supplementary Fig. 7b). This suggests that wind-forced thermocline displacement may play a central role in forming subsurface temperature anomalies in the off-equatorial western Pacific at the decadal timescale.

We then investigate the role of TPDV-related wind forcing in driving off-equatorial thermocline variability. Figure 4b shows the regression of area-averaged temperature anomalies between 22 and 24.5σ_θ in the NW box upon the filtered SLP and 10-m wind anomalies. Similar to Fig. 3a, the strong positive SST anomalies in the central equator induce a band of positive (negative) SLP anomalies in the west (east). The resulting cyclonic circulation in the northwest (southwest) produces strong northwesterly (southwesterly) winds equatorward of 15°N (15°S) (Figs. 3a, 4b) with associated positive (negative) wind stress curl anomalies in the north (south) western Pacific (Supplementary Fig. 4a, c). Consequently, the positive Ekman pumping (Supplementary Fig. 4b, d) induces surface divergence and generates negative subsurface temperature anomalies in the off-equatorial western Pacific (Fig. 3i). We further quantify the impacts of local wind forcing on subsurface temperature changes through the lead-lag correlation between Ekman pumping and subsurface temperature anomalies averaged in the NW box at interannual (Supplementary Fig. 8, gray line) and decadal (Supplementary Fig. 9, gray line) timescales. At both timescales, the contribution of Ekman pumping to subsurface temperature changes is strong, particularly at low-frequency bands[67] (correlation coefficient reaches 0.88 when Ekman pumping leads subsurface temperature by 13 months), highlighting the crucial role of local wind forcing in the formation of NW box subsurface temperature anomalies.

Apart from the impacts of local wind forcing, thermocline displacements-induced subsurface temperature anomalies may potentially result from westward propagating oceanic Rossby waves originating in the off-equatorial eastern basin[41,49,67]. Supplementary Fig. 10 depicts the connection between NW box subsurface temperature anomalies and SSH variability averaged across different longitudinal bands in the North Pacific. Noticeable SSH signals capable of reaching the western boundary are primarily observed west of 160°W (Supplementary Fig. 10b–e). The estimated speed of Rossby wave propagation from 160°W to 160°E is approximately 14–17 cm/s at 13°N, qualitatively aligning with previous findings[41]. At 6°N, the speed of Rossby wave propagation is much faster, requiring fewer months to reach the western boundary from 160°W.

To further assess the impact of Rossby wave-induced subsurface temperature anomalies, we calculate lead-lag correlation coefficients between NW box subsurface temperature and SSH anomalies averaged across different longitudinal bands (Supplementary Figs. 8 and 9). At timescales shorter than a year, SSH variability west of 170°W exhibits a strong correlation with changes in NW box subsurface temperature, leading by approximately one month (black line in Supplementary Fig. 8, correlation coefficient reaches 0.56), consistent with the estimated cross-basin timescale depicted in Supplementary Fig. 10e. In contrast, east of 170°W the correlation diminishes significantly, suggesting that Rossby waves originating in the off-equatorial eastern Pacific are not the primary contributor to

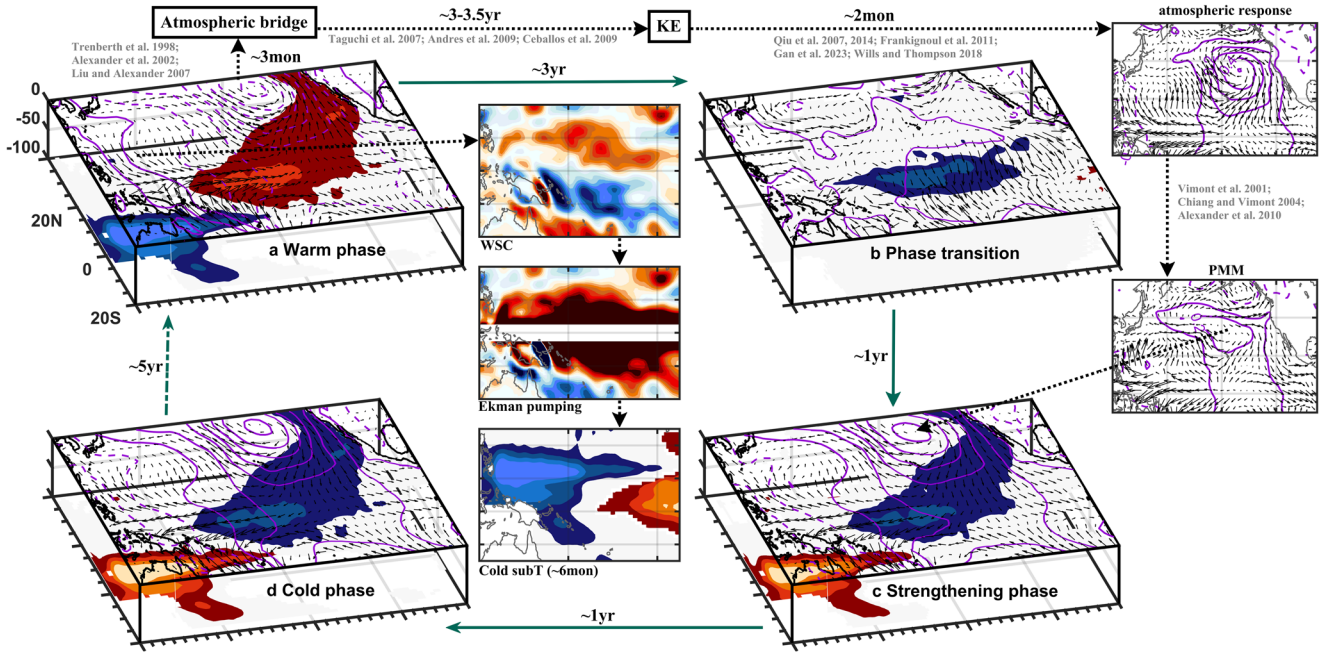

Fig. 6 | Off-equatorial subsurface temperature anomalies and extratropical-tropical ocean-atmosphere interaction determine the preferred timescale of TPDV. a Warm phase of TPDV is characterized by the strongest surface warming in the Niño4 region, off-equatorial western Pacific Gill-response and strong subsurface cooling, and extratropical cyclonic circulation. **b** Surfacing of off-equatorial northwestern subsurface temperature anomalies in the Niño4 region. **c** PMM (with contribution from KE) enhances the subsurface-produced equatorial disturbance in the Niño4 region. **d** Same as the warm phase but the sign reversed.

interannual subsurface temperature changes in the off-equatorial northwestern Pacific. However, at decadal timescales, SSH variability east of 170°W is predominantly out of phase with changes in NW box subsurface temperature anomalies while west of 170°W the correlation between SSH anomalies and subsurface temperature weakens (Supplementary Fig. 9). These findings indicate that off-equatorial Rossby waves do not play a central role in driving subsurface temperature changes in the northwestern Pacific at the decadal timescale. Consequently, the primary contributor to decadal-scale NW box subsurface temperature anomalies appears to be local wind forcing rather than Rossby wave propagation (Supplementary Fig. 9, comparing the gray line and black line at negative lags).

The negative temperature anomalies in the off-equatorial southwestern Pacific are relatively weaker compared to the northern counterpart (Fig. 3i). While previous modeling studies[68] and observational analysis[33] have suggested the critical role of the South Pacific in driving the phase transition of the TPDV, we highlight the larger contribution from the northern hemisphere than the southern part. This difference can be attributed to two main causes. Firstly, the use of shallower isopycnal levels in our analysis effectively captures the direct impact of subsurface anomalies on Niño4 surface temperature variability. This contrasts with previous studies based on deeper isopycnal levels[33,68]. Consequently, our framework aligns with the observed decadal timescale oscillation (Figs. 1 and 2) rather than the approximately 14-year periods found in previous observational study[33]. Secondly, our analysis is consistent with recent findings that the off-equatorial northwestern Pacific plays a more substantial role in the equatorial heat budget at the decadal timescale[49,69]. Furthermore, the weaker signal in the southwestern Pacific might be related to the structure of the wind forcing. Specifically, the zonal coherency of the Ekman pumping has been proposed as the primary factor determining the low-frequency variability while local maxima of the forcing only affects the sharpness of the variability[67]. In Fig. 4d, the northern off-equatorial Ekman pumping is elongated from around 130°W to the western boundary while the southern off-equatorial Ekman pumping is only extended from around 140°W to 150°E with the occurrence of a band of negative Ekman pumping centered around 10°S and 150°E. Therefore, the specific structure of the forcing might be a significant factor explaining the weaker signal from the South Pacific in the TPDV.

Overall TPDV framework with phase reversal

The decadal oscillation framework in the tropical Pacific can be summarized as follows:

(a) Positive phase. strongest positive temperature anomalies in the Niño4 region (Figs. 3a, 6a). Ensemble atmospheric modeling experiments with prescribed additional 2 °C SST forcing (see Methods) further confirm that surface warming in the Niño4 region can induce cyclonic circulation in the northwestern and southwestern Pacific (Fig. 4e, g), respectively, leading to the corresponding positive and negative wind stress curl anomalies in the 2–15°N and 2–15°S latitudinal bands (Supplementary Fig. 4a, c). The resulting positive Ekman pumping (Supplementary Fig. 4b, d) drives negative subsurface temperature with the strongest signals in the off-equatorial northwestern Pacific (Fig. 3i). This is also confirmed by the ensemble oceanic modeling experiments when TPDV-associated wind fields (Fig. 3a) were prescribed (Fig. 4f, h).

(b) Transition phase. Off-equatorial northwestern subsurface temperature anomalies gradually migrate toward the central basin along the NECC pathway (Fig. 5a–f and Supplementary Fig. 6). As the isopycnal shoals toward the east, negative subsurface temperature anomalies are accumulated in the Niño4 region around three years later (Figs. 3d, l and 6b).

(c) Strengthening phase. During the positive phase of TPDV, warming in the equatorial central Pacific triggers a train of atmospheric Rossby waves to induce extratropical atmospheric circulation anomalies (around 3 months)[42–44], driving the westward propagating oceanic Rossby waves that affect the KE system (around 2.5–3 years)[25,56–58]. The change of the KE state then induces a downstream atmospheric response that projects onto the forcing pattern of the PMM[62] (Supplementary Fig. 5). The PMM further strengthens the subsurface-induced

SST anomalies in the central equatorial Pacific 0–12 months before the peak of the cold phase (Figs. 3f–h and 6c)[24].

(d) Cold phase. The accumulation of subsurface temperature anomalies in the Niño4 region originated from the off-equatorial northwestern Pacific subsurface anomalies, along with the enhancement of the KE and thus PMM contribution, result in the cold phase of TPDV after around 5–6 years (Figs. 3h and 6d), setting up a half cycle of the decadal oscillation. The remaining opposite cycle is simply the reverse of the processes mentioned above (Fig. 6).

Discussion

Based on available observational and reanalysis products and ensemble model experiments, this study presents a modified framework of TPDV involving off-equatorial subsurface temperature anomalies and extratropical-tropical ocean-atmosphere interaction. The combined contribution of off-equatorial subsurface temperature propagation and PMM eventually leads to the mature cold phase after five years. The center of equatorial negative SST anomalies then forces anomalous atmospheric circulation, resulting in positive subsurface temperature anomalies in the off-equatorial western area and potentially reversing the state of TPDV. Thus, a periodic oscillation of around 10 years is achieved.

The impact of the PMM in strengthening TPDV during the transition state remains a subject of debate. A recent study indicated that while the causal relationship between PMM and TPDV is apparent, the influence of PMM might have been overestimated in the previous literature[70]. Further analysis is required to investigate the extent to which PMM contributes to the strengthening of equatorial SST anomalies during the transition state. Another noteworthy issue concerns the decadal phase change of PMM. While KE can partially explain PMM forcing, uncertainties persist regarding whether PMM is influenced by factors within and/or outside the Pacific. Some studies indicate that the decadal PMM is primarily driven by a tripole mode pattern of SLP anomalies extending from northeastern Asia to the northeastern Pacific[54]. Conversely, others suggest that the positive phase of the Atlantic Multidecadal Oscillation can weaken the Aleutian Low via atmospheric teleconnection, thereby contributing to PMM[71]. Further investigations are necessary to discern the fraction of decadal PMM variability driven by intra-basin factors versus inter-basin factors. Moreover, it is crucial to explore how these physical processes activate the preferred decadal time-scale variability of PMM. Unraveling the intricacies of the decadal phase change of PMM extends beyond the scope of the present study and may be explored more thoroughly in our future research.

TPDV-associated SST anomalies can induce extratropical anomalous wind fields, generating off-equatorial Rossby waves in both the North and South Pacific. These waves then propagate westward and may potentially contribute to the phase transition of TPDV[49,72]. We show the temporal evolution of SSH anomalies along a specific circuit[41], westward along 13°N (Supplementary Fig. 11a), then equatorward along the western boundary at 130°E (Supplementary Fig. 11b), and eastward along the equator (Supplementary Fig. 11c). Most of the SSH anomalies originating west of 160°W appear to reach the western boundary at 13°N after 2–3 years (Supplementary Fig. 11a), then follow the western boundary to reach the equatorial western Pacific (Supplementary Fig. 11b), and propagate eastward to the central basin along the equator at much-reduced amplitude (Supplementary Fig. 11c). Along the equator, we also observe the propagating SSH signals disconnect abruptly around 160°E, suggesting that off-equatorial Rossby waves might not be the primary contributor to the phase reversal of TPDV (Supplementary Fig. 11d, e). Furthermore, a recent study postulated that robust ENSO events could potentially influence the phase transition of TPDV[49]. However, we have identified only two distinct ENSO events that could play a role in the phase transition of TPDV within the scope of our analysis: the 1965/66 El Niño and 2007/08 La Niña (Supplementary Fig. 11d, e). The former may contribute to the transition from a negative to a positive phase, while the latter may contribute to the transition from a positive to a negative phase of TPDV. Nonetheless, a more comprehensive analysis is necessary to accurately quantify the degree to which ENSO events contribute to the phase transition of TPDV.

Methods

Observational and reanalysis datasets

For subsurface temperature and salinity, we utilize the latest EN.4.2.2 (EN422) from the Met Office Hadley Centre[73]. The EN422 has four ensemble members which are different in the scheme used to adjust bias in Mechanical Bathythermograph and Expendable Bathythermographs data. These ensembles are distributed on a 1° horizontal resolution over 42 irregularly spaced depth levels spanning from 1900 to present at monthly intervals. The ensemble of EN.4.2.2.analyses.g10 from 1950 to 2021 is used here. Similar results are obtained in the other three ensembles. For the SSH data, the Estimating the Circulation and Climate of the Ocean project, version 3 (GECCO3)[74] is utilized. This data set has 1° horizontal resolutions and 40 vertical levels from 1948 to 2018. For the ocean currents, the Global Ocean Data Assimilation System (GODAS)[75,76] with 0.33° latitude×1° longitude during 1980–2020 is used.

For atmospheric variables, monthly SLP and 10-m winds are from the National Centers for Environmental Prediction-National Center for Atmospheric Research Reanalysis 1 dataset[77]. These data are distributed on a 2.5° × 2.5° latitude-longitude grid, covering the period from 1948 to the present. In addition, the global 1° gridded monthly SST from the Hadley Centre Global Sea Ice and Sea Surface Temperature (HadISST)[78] dataset is used.

Subsurface temperature coordinate transformation and NECC pathway

All data are linearly detrended before conducting analyses and anomalies are defined as deviations from the climatology of the whole period of the respective dataset. As the focus of the study is on the decadal timescale, an 8–20 year Lanczos bandpass filter is used[79]. For subsurface data, the temperature on pressure coordinates is converted to time-mean sigma coordinates with an increment of 0.02 kgm^{-3} by linear interpolation (the resulting isopycnal temperature is not necessarily salinity compensated). We then define two isopycnal ranges of the 22–24.5 σ_θ and 24.5–26 σ_θ to identify the origin of the TPDV. This separation aims to quantify the former as the tropical origin[66] and the latter as extratropical origin[34] (Supplementary Fig. 2). Our result is similar regardless of the chosen upper isopycnal ranges (22.4–24.5 σ_θ, 22.5–24.5 σ_θ or 23–24.5 σ_θ) as well as lower isopycnals (24.5–25.5 σ_θ, 25–25.5 σ_θ or 25–26 σ_θ). The ocean pathway is represented by the mean acceleration potential[80] (the geostrophic streamfunction for flow in a specific volume anomaly surface) referenced to 1000 dbar and mean currents evaluated on the isopycnal surface.

Wavelet analysis

As the widely used Morlet wavelet analysis[81] exhibits bias in the estimate of wavelet power spectra of geophysical time series, we use the bias-rectified wavelet approach[45]. We also perform wavelet coherence analysis[82] to detect the phase relationship between surface and subsurface variability in the Niño4 region.

MTM-SVD

We employ the MTM-SVD which is a powerful multivariate signal processing method ideal for extracting narrowband spatial-temporal variability in a red noise background[83,84]. The feature of decadal variability is then explored by performing MTM-SVD analysis of joint normalized raw detrended oceanic and atmospheric fields in the domain of 40°S–40°N and 120°E–80°W. Our result is not sensitive to the domain or combined fields used for the analysis. The MTM-SVD analysis was performed using $K = 3$ data tapers (windowing functions) and a time-frequency bandwidth product of $NW = 2$. The significant level of the resulting LFV spectrum is estimated by 300 synthetic time series of the original dataset obtained by temporal shuffling. The 95% confidence level is used to distinguish the LFV peak from the "locally white" noise background.

Random phase test

To identify the causal relationship between the fields, lagged correlation and regression are used. Because bandpass filtering strongly reduces the effective sample size of the time series and the degree of reduction is hard to estimate accurately, we use a non-parameter method (random-phase)[85] to test the significance of our statistical analysis. Supposedly, r(A, B) is the regression between two time series A and B at a certain lag. The statistical significance of regression can be tested via two steps. First is the generation of 8000 synthetic time series from A that has the same length and same power spectrum but differences in temporal phases. Second, we calculate the lagged regression of the reconstructed time series with B. If the magnitude of r(A, B) is equal to or greater than a certain percentage (at least 90% in this study) of the regressions from the random-phase time series, we assume that r(A, B) passes the confidence level.

Lagrangian particle-tracking experiments

To verify the NECC pathway and the associated propagation timescale, we conducted offline Lagrangian particle-tracking simulations using the long-term monthly mean currents from GODAS during 1980–2021. Particles were initialized at various isopycnal surfaces (22.5 σ_θ, 23 σ_θ, 23.5 σ_θ, and 24 σ_θ) within the region of 4°–6°N and 140°–160°E to ensure the robustness of our analysis. A total of 24,000 particles were released for each isopycnal surface, starting in January.

Numerical experiment

The dynamical processes involved in our analysis are further confirmed using the numerical experiments based on the Community Earth System Model (CESM) version 1.2.2. To verify the role of TPDV-induced anomalous atmospheric circulation (Gill-type response in the off-equatorial western Pacific), we conduct the specified SST anomaly experiments with the Community Atmospheric Model version 5 (CAM5). The prescribed heat source is within the region 5°S–5°N, 160°E–160°W while outside this domain the SST is nudged toward climatological value[49,69]. We add 2 °C SST to the climatological value within the defined region. The experiment is run for 30 years. The anomalies are then defined as deviations from a 30-year control run with specified climatological SST.

We also perform a 10-member ensemble run of the prescribed 2 °C SST value in the region mentioned above. Each ensemble member is slightly different in the initial condition by randomly imposing small perturbations to the initial temperature fields. Specifically, we set the CESM1.2.2 namelist variable "pertlim" ranging from 1×10^{-14} to 10×10^{-14}. All ensemble members are then run for 10 years and anomalies are defined as deviations from a 30-year control run with specified climatological SST.

To demonstrate the role of TPDV-induced off-equatorial subsurface temperature anomalies, the Pacific anomalous wind field associated with the positive phase of TPDV (Fig. 3a) is superimposed to force the Parallel Ocean Program version 2 (POP2)[86]. We perform a 15-member ensemble run which is different slightly in the perturbation in addition to the added TPDV anomalous wind field. The imposed wind field is as follows,

$$\textit{Imposed wind field} = \textit{Climatological wind} + \textit{TPDV associated wind} + \textit{Perturbed wind}$$

where the perturbed wind is generated by a random matrix of predefined coefficients (ranging from 0.0001 to 0.0005). We choose to perturb the 10-m wind field in the zonal, meridional, and both directions corresponding to the defined coefficients. Each ensemble member is run for 30 years and anomalies are defined as departures from the 100-year control run with normal year forcing. All the statistical significance of the modeling results is based on a Student's *t* test.

Data availability

The thermodynamic Equation of Seawater 2020 (TEOS-10) https://www.teos-10.org/ The wavelet packages https://paos.colorado.edu/research/wavelets/ The rectified wavelet codes http://ocgweb.marine.usf.edu/~liu/wavelet.html The wavelet coherence codes www.pol.ac.uk/home/research/waveletcoherence/ The MTM-SVD code http://www.meteo.psu.edu/holocene/public_html/supplements/Mann_MTMSVD_2020/Code/ The PMM index https://www.aos.wisc.edu/~dvimont/MModes/RealTime/PMM.RAW.txt The CESM1.2.2 code https://www2.cesm.ucar.edu/models/cesm1.2/ Links to datasets used: HadISST1: https://www.metoffice.gov.uk/hadobs/hadisst/ NCEP-NCAR Reanalysis 1: https://psl.noaa.gov/data/gridded/data.ncep.reanalysis.html EN422: https://www.metoffice.gov.uk/hadobs/en4/download-en4-2-2.html GECCO3: https://www.cen.uni-hamburg.de/en/icdc/data/ocean/reanalysis-ocean/gecco3.html GODAS: https://psl.noaa.gov/data/gridded/data.godas.html.

Code availability

Any relevant codes necessary to reproduce the results presented in this study are available from the corresponding author upon request.

Received: 31 October 2023; Accepted: 10 April 2024;
Published online: 22 May 2024

References

1. Tourre, Y. M., Rajagopalan, B., Kushnir, Y., Barlow, M. & White, W. B. Patterns of coherent decadal and interdecadal climate signals in the Pacific Basin during the 20th century. *Geophys. Res. Lett.* **28**, 2069–2072 (2001).
2. Liu, Z. Dynamics of interdecadal climate variability: a historical perspective. *J. Clim.* **25**, 1963–1995 (2012).
3. Power, S. et al. Decadal climate variability in the tropical Pacific: characteristics, causes, predictability, and prospects. *Science* **374**, eaay9165 (2021).
4. Di Lorenzo, E. et al. Modes and mechanisms of pacific decadal-scale variability. *Annu. Rev. Mar. Sci.* **15**, 249–275 (2023).
5. Capotondi, A. et al. Mechanisms of tropical Pacific decadal variability. *Nat. Rev. Earth Environ.* **4**, 754–769 (2023).
6. Okumura, Y. M., DiNezio, P. & Deser, C. Evolving impacts of multiyear La Niña events on atmospheric circulation and U.S. Drought. *Geophys. Res. Lett.* **44**, 11,614–11,623 (2017).
7. Zhang, W. et al. Unraveling El Niño's impact on the East Asian Monsoon and Yangtze River summer flooding. *Geophys. Res. Lett.* **43**, 11,375–11,382 (2016).
8. Timmermann, A. et al. El Niño–Southern oscillation complexity. *Nature* **559**, 535–545 (2018).
9. Liu, Z. & Di Lorenzo, E. Mechanisms and predictability of pacific decadal variability. *Curr. Clim. Change Rep.* **4**, 128–144 (2018).
10. Zhao, Y. & Di Lorenzo, E. The impacts of Extra-tropical ENSO precursors on tropical pacific decadal-scale variability. *Sci. Rep.* **10**, 3031 (2020).
11. Power, S., Casey, T., Folland, C., Colman, A. & Mehta, V. Inter-decadal modulation of the impact of ENSO on Australia. *Clim. Dyn.* **15**, 319–324 (1999).
12. Sullivan, A. et al. Robust contribution of decadal anomalies to the frequency of central-Pacific El Niño. *Sci. Rep.* **6**, 38540 (2016).
13. Zhang, Y., Wallace, J. M. & Battisti, D. S. ENSO-like interdecadal variability: 1900–93. *J. Clim.* **10**, 1004–1020 (1997).
14. Newman, M. et al. The Pacific decadal oscillation, revisited. *J. Clim.* **29**, 4399–4427 (2016).
15. Kleeman, R., McCreary, J. P. Jr. & Klinger, B. A. A mechanism for generating ENSO decadal variability. *Geophys. Res. Lett.* **26**, 1743–1746 (1999).
16. Liu, C., Zhang, W., Jin, F.-F., Stuecker, M. F. & Geng, L. Equatorial origin of the observed tropical pacific quasi-decadal variability from ENSO nonlinearity. *Geophys. Res. Lett.* **49**, e2022GL097903 (2022).
17. Ashok, K., Behera, S. K., Rao, S. A., Weng, H. & Yamagata, T. El Niño Modoki and its possible teleconnection. *J. Geophys. Res. Oceans*. **112**, C11007 (2007).

18. Capotondi, A., Newman, M., Xu, T. & Di Lorenzo, E. An optimal precursor of northeast Pacific marine heatwaves and central Pacific El Niño events. *Geophys. Res. Lett.* **49**, e2021GL097350 (2022).
19. Chiang, J. C. H. & Vimont, D. J. Analogous Pacific and Atlantic Meridional modes of tropical atmosphere–ocean variability. *J. Clim.* **17**, 4143–4158 (2004).
20. Stuecker, M. F. Revisiting the Pacific Meridional Mode. *Sci. Rep.* **8**, 3216 (2018).
21. Chunhan, J., Bin, W. & Jian, L. Emerging Pacific quasi-decadal oscillation over the past 70 Years. *Geophys. Res. Lett.* **48**, e2020GL090851 (2021).
22. Vimont, D. J. The Contribution of the interannual ENSO cycle to the spatial pattern of decadal ENSO-Like variability. *J. Clim.* **18**, 2080–2092 (2005).
23. Rodgers, K. B., Friederichs, P. & Latif, M. Tropical Pacific decadal variability and its relation to decadal modulations of ENSO. *J. Clim.* **17**, 3761–3774 (2004).
24. Di Lorenzo, E. et al. ENSO and meridional modes: a null hypothesis for Pacific climate variability. *Geophys. Res. Lett.* **42**, 9440–9448 (2015).
25. Joh, Y., & Di Lorenzo, E. Interactions between Kuroshio Extension and Central Tropical Pacific lead to preferred decadal-timescale oscillations in Pacific climate. *Sci. Rep.* **9**, 13558 (2019).
26. Zhao, Y., Di Lorenzo, E., Newman, M., Capotondi, A. & Stevenson, S. A pacific tropical decadal variability challenge for climate models. *Geophys. Res. Lett.* **50**, e2023GL104037 (2023).
27. Schneider, N., Miller, A. J., Alexander, M. A. & Deser, C. Subduction of decadal north pacific temperature anomalies: observations and dynamics. *J. Phys. Oceanogr.* **29**, 1056–1070 (1999).
28. McCreary, J. P. & Lu, P. Interaction between the subtropical and equatorial ocean circulations: the subtropical cell. *J. Phys. Oceanogr.* **24**, 466–497 (1994).
29. Gu, D. & Philander, S. G. H. Interdecadal climate fluctuations that depend on exchanges between the tropics and extratropics. *Science* **275**, 805–807 (1997).
30. Kolodziejczyk, N. & Gaillard, F. Observation of spiciness interannual variability in the Pacific pycnocline. *J. Geophys. Res. Oceans*. **117**, C12018 (2012).
31. Yeager, S. G. & Large, W. G. Late-winter generation of spiciness on subducted isopycnals. *J. Phys. Oceanogr.* **34**, 1528–1547 (2004).
32. San, S.-C. & Tseng, Y.-h. Aleutian low/PDO forces a decadal subsurface spiciness propagating mode in the North Pacific. *Clim. Dyn*. **62**, 703–721 (2024).
33. Luo, J.-J. & Yamagata, T. Long-term El Niño-Southern Oscillation (ENSO)-like variation with special emphasis on the South. *Pac. J. Geophys. Res. Oceans* **106**, 22211–22227 (2001).
34. Zeller, M., McGregor, S., van Sebille, E., Capotondi, A. & Spence, P. Subtropical-tropical pathways of spiciness anomalies and their impact on equatorial Pacific temperature. *Clim. Dyn.* **56**, 1131–1144 (2021).
35. Capotondi, A., Alexander, M. A., Deser, C. & McPhaden, M. J. Anatomy and decadal evolution of the pacific Subtropical–Tropical Cells (STCs). *J. Clim.* **18**, 3739–3758 (2005).
36. Liu, Z., Philander, S. G. H. & Pacanowski, R. C. A GCM study of tropical–subtropical upper-ocean water exchange. *J. Phys. Oceanogr.* **24**, 2606–2623 (1994).
37. McPhaden, M. J. & Zhang, D. Pacific ocean circulation rebounds. *Geophys. Res. Lett*. **31**, L18301 (2004).
38. Solomon, A., McCreary, J. P., Kleeman, R. & Klinger, B. A. Interannual and decadal variability in an intermediate coupled model of the pacific region. *J. Clim.* **16**, 383–405 (2003).
39. Cheng, W., McPhaden, M. J., Zhang, D. & Metzger, E. J. Recent changes in the pacific subtropical cells inferred from an eddy-resolving ocean circulation model. *J. Phys. Oceanogr.* **37**, 1340–1356 (2007).
40. Capotondi, A. & Qiu, B. Decadal variability of the pacific shallow overturning circulation and the role of local wind forcing. *J. Clim*. **36**, 1001–1015 (2023).
41. Capotondi, A. & Alexander, M. A. Rossby waves in the tropical north pacific and their role in decadal thermocline variability. *J. Phys. Oceanogr.* **31**, 3496–3515 (2001).
42. Alexander, M. A. et al. The atmospheric bridge: the influence of ENSO teleconnections on Air–Sea interaction over the Global Oceans. *J. Clim.* **15**, 2205–2231 (2002).
43. Liu, Z. & Alexander, M. Atmospheric bridge, oceanic tunnel, and global climatic teleconnections. *Rev. Geophys*. **45**, RG2005 (2007).
44. Trenberth, K. E. et al. Progress during TOGA in understanding and modeling global teleconnections associated with tropical sea surface temperatures. *J. Geophys. Res. Oceans* **103**, 14291–14324 (1998).
45. Liu, Y., San Liang, X. & Weisberg, R. H. Rectification of the Bias in the Wavelet Power Spectrum. *J. Atmos. Ocean. Technol.* **24**, 2093–2102 (2007).
46. Lyu, K., Zhang, X., Church, J. A., Hu, J. & Yu, J.-Y. Distinguishing the Quasi-Decadal and multidecadal sea level and climate variations in the pacific: implications for the ENSO-like low-frequency variability. *J. Clim.* **30**, 5097–5117 (2017).
47. Zhang, Y. et al. Atmospheric forcing of the pacific meridional mode: tropical pacific-driven versus internal variability. *Geophys. Res. Lett.* **49**, e2022GL098148 (2022).
48. Zhang, H., Clement, A., & Di Nezio, P. The South Pacific meridional mode: a mechanism for ENSO-like variability. *J. Clim.* **27**, 769–783 (2014).
49. Meehl, G. A., Teng, H., Capotondi, A. & Hu, A. The role of interannual ENSO events in decadal timescale transitions of the Interdecadal Pacific Oscillation. *Clim. Dyn.* **57**, 1933–1951 (2021).
50. Vimont, D. J., Battisti, D. S. & Hirst, A. C. Footprinting: a seasonal connection between the tropics and mid-latitudes. *Geophys. Res. Lett.* **28**, 3923–3926 (2001).
51. Alexander, M. A., Vimont, D. J., Chang, P. & Scott, J. D. The impact of extratropical atmospheric variability on ENSO: testing the seasonal footprinting mechanism using coupled model experiments. *J. Clim.* **23**, 2885–2901 (2010).
52. Alexander, M. Extratropical Air-Sea Interaction, Sea Surface Temperature Variability, and the Pacific Decadal Oscillation. *Clim. Dyn. Why Does Climate Vary?* (eds Sun, D.-Z. & Bryan, F.) 123–148 (2010).
53. Pierce, D. W. Distinguishing coupled ocean–atmosphere interactions from background noise in the North Pacific. *Prog. Oceanogr.* **49**, 331–352 (2001).
54. Zhang, Y. et al. Pacific meridional modes without equatorial pacific influence. *J. Clim.* **34**, 5285–5301 (2021).
55. Tseng, Y.-h, Ding, R., Zhao, S., Kuo, Y.-c & Liang, Y.-c. Could the North Pacific oscillation be modified by the initiation of the east asian winter monsoon? *J. Clim.* **33**, 2389–2406 (2020).
56. Ceballos, L. I., Di Lorenzo, E., Hoyos, C. D., Schneider, N. & Taguchi, B. North Pacific gyre oscillation synchronizes climate fluctuations in the eastern and western boundary systems. *J. Clim.* **22**, 5163–5174 (2009).
57. Taguchi, B. et al. Decadal variability of the Kuroshio extension: observations and an Eddy-Resolving model hindcast. *J. Clim.* **20**, 2357–2377 (2007).
58. Andres, M. et al. Manifestation of the pacific decadal oscillation in the Kuroshio. *Geophys. Res. Lett*. **36**, L16602 (2009).
59. Qiu, B., Chen, S., Schneider, N. & Taguchi, B. A coupled decadal prediction of the dynamic State of the Kuroshio extension system. *J. Clim.* **27**, 1751–1764 (2014).
60. Qiu, B., Schneider, N. & Chen, S. Coupled decadal variability in the North Pacific: an observationally constrained idealized model. *J. Clim.* **20**, 3602–3620 (2007).

61. Frankignoul, C., Sennéchael, N., Kwon, Y.-O. & Alexander, M. A. Influence of the Meridional Shifts of the Kuroshio and the Oyashio extensions on the atmospheric circulation. *J. Clim.* **24**, 762–777 (2011).
62. Gan, B. et al. A Mesoscale ocean–atmosphere coupled pathway for decadal variability of the kuroshio extension system. *J. Clim.* **36**, 485–510 (2023).
63. Wills, S. M. & Thompson, D. W. J. On the observed relationships between Wintertime Variability in Kuroshio–Oyashio extension sea surface temperatures and the atmospheric circulation over the North Pacific. *J. Clim.* **31**, 4669–4681 (2018).
64. Zhang, R.-H. & Rothstein, L. M. Role of off-equatorial subsurface anomalies in initiating the 1991–1992 El Niño as revealed by the National Centers for Environmental Prediction ocean reanalysis data. *J. Geophys. Res. Oceans* **105**, 6327–6339 (2000).
65. Zhang, R.-H., Rothstein, L. M., Busalacchi, A. J. & Liang, X.-Z. The onset of the 1991–92 El Niño event in the tropical Pacific Ocean: the NECC subsurface pathway. *Geophys. Res. Lett.* **26**, 847–850 (1999).
66. Schneider, N. A decadal spiciness mode in the tropics. *Geophys. Res. Lett.* **27**, 257–260 (2000).
67. Capotondi, A., Alexander, M. A. & Deser, C. Why are there rossby wave maxima in the Pacific at 10°S and 13°N? *J. Phys. Oceanogr.* **33**, 1549–1563 (2003).
68. Cibot, C., Maisonnave, E., Terray, L. & Dewitte, B. Mechanisms of tropical Pacific interannual-to-decadal variability in the ARPEGE/ ORCA global coupled model. *Clim. Dyn.* **24**, 823–842 (2005).
69. Meehl, G. A., Hu, A. & Teng, H. Initialized decadal prediction for transition to positive phase of the Interdecadal Pacific Oscillation. *Nat. Commun.* **7**, 11718 (2016).
70. Hu, R., Lian, T., Feng, J. & Chen, D. Pacific meridional mode does not induce strong positive SST anomalies in the central equatorial Pacific. *J. Clim*. **36**, 4113–4131 (2023).
71. Sun, C. et al. Western tropical Pacific multidecadal variability forced by the Atlantic multidecadal oscillation. *Nat. Commun.* **8**, 15998 (2017).
72. Meehl, G. A. & Hu, A. Megadroughts in the Indian Monsoon region and Southwest North America and a mechanism for associated multidecadal pacific sea surface temperature anomalies. *J. Clim.* **19**, 1605–1623 (2006).
73. Good, S. A., Martin, M. J. & Rayner, N. A. EN4: quality controlled ocean temperature and salinity profiles and monthly objective analyses with uncertainty estimates. *J. Geophys. Res. Oceans* **118**, 6704–6716 (2013).
74. Köhl, A. Evaluating the GECCO3 1948–2018 ocean synthesis – a configuration for initializing the MPI-ESM climate model. *Q. J. R. Meteorol. Soc.* **146**, 2250–2273 (2020).
75. Behringer, D. W., Ji, M. & Leetmaa, A. An improved coupled model for ENSO prediction and implications for ocean initialization. Part I: the ocean data assimilation system. *Monthly Weather Rev.* **126**, 1013–1021 (1998).
76. Behringer, D. W. & Xue, Y. Evaluation of the global ocean data assimilation system at NCEP: the Pacific Ocean. Eighth Symposium on Integrated Observing and Assimilation Systems for Atmosphere, Oceans, and Land Surface. AMS (2004).
77. Kalnay, E. et al. The NCEP/NCAR 40-Year Reanalysis Project. *Bull. Am. Meteorol. Soc.* **77**, 437–472 (1996).
78. Rayner, N. A. et al. Global analyses of sea surface temperature, sea ice, and night marine air temperature since the late nineteenth century. *J. Geophys. Res. Atmos*. **108**, 4407 (2003).
79. Duchon, C. E. Lanczos filtering in one and two dimensions. *J. Appl. Meteorol. Climatol.* **18**, 1016–1022 (1979).
80. McDougall, T. J. & Klocker, A. An approximate geostrophic streamfunction for use in density surfaces. *Ocean Model.* **32**, 105–117 (2010).
81. Torrence, C. & Compo, G. P. A practical guide to wavelet analysis. *Bull. Am. Meteorol. Soc.* **79**, 61–78 (1998).
82. Grinsted, A., Moore, J. C. & Jevrejeva, S. Application of the cross wavelet transform and wavelet coherence to geophysical time series. *Nonlin. Process. Geophys* **11**, 561–566 (2004).
83. Mann, M. E. & Park, J. Oscillatory spatiotemporal signal detection in climate studies: a multiple-taper spectral domain approach. *Adv. Geophys.* **41**, 1–131 (1999).
84. Mann, M. E. & Park, J. Global-scale modes of surface temperature variability on interannual to century timescales. *J. Geophys. Res. Atmos.* **99**, 25819–25833 (1994).
85. Ebisuzaki, W. A method to estimate the statistical significance of a correlation when the data are serially correlated. *J. Clim.* **10**, 2147–2153 (1997).
86. Smith, R. et al. The parallel ocean program (POP) reference manual ocean component of the community climate system model (CCSM) and community earth system model (CESM). *LAUR-01853* **141**, 1–140 (2010).

Acknowledgements

The authors extend sincere thanks to Prof. Chung-Hsiung Sui and Prof. Fei-Fei Jin for insightful comments and suggestions. Computational resources were provided by the National Center for High-performance Computing (NCHC) of the National Applied Research Laboratories (NARLabs) in Taiwan. This research was supported by the NSTC Grant 112-2611-M-002-016-MY3, Taiwan.

Author contributions

S.-C.S. and Y.-H.T. designed the study. S.-C.S. conducted data analyses, prepared all figures, performed the modeling experiments, and drafted the paper. S.-C.S. and Y.-H.T. discussed the results and contributed to manuscript writing. R.Q.D. and E.D.L. assisted in interpreting the results and improving the manuscript.

Competing interests

The authors declare no competing interests.

Additional information

Supplementary information The online version contains supplementary material available at https://doi.org/10.1038/s41612-024-00643-z.

Correspondence and requests for materials should be addressed to Yu-Heng Tseng.

Reprints and permissions information is available at http://www.nature.com/reprints

Publisher's note Springer Nature remains neutral with regard to jurisdictional claims in published maps and institutional affiliations.

Open Access This article is licensed under a Creative Commons Attribution 4.0 International License, which permits use, sharing, adaptation, distribution and reproduction in any medium or format, as long as you give appropriate credit to the original author(s) and the source, provide a link to the Creative Commons licence, and indicate if changes were made. The images or other third party material in this article are included in the article's Creative Commons licence, unless indicated otherwise in a credit line to the material. If material is not included in the article's Creative Commons licence and your intended use is not permitted by statutory regulation or exceeds the permitted use, you will need to obtain permission directly from the copyright holder. To view a copy of this licence, visit http://creativecommons.org/licenses/by/4.0/.

© The Author(s) 2024